A neutron Brillouin scattering study of $Mg_{70}Zn_{30}$

1995 J. Phys.: Condens. Matter 7 4775

(http://iopscience.iop.org/0953-8984/7/25/004)

J. Phys.: Condens. Matter 7 (1995) 4775–4785. Printed in the UK

A neutron Brillouin scattering study of $Mg_{70}Zn_{30}$

C J Benmore†, B J Oliver‡¶, J-B Suck§, R A Robinson‡ and P A Egelstaff†

† Department of Physics, University of Guelph, Guelph, Ontario N1G 2W1, Canada
‡ Los Alamos National Laboratory, LANSCE, Los Alamos, NM 87545, USA
§ Institut Laue-Langevin, BP156 F-38042 Grenoble Cédex 9, France

Received 3 February 1995

Abstract. Inelastic neutron scattering measurements have been made with momentum transfers within the first pseudo-Brillouin zone of a magnesium/zinc glass at 100 K and 297 K. We describe the application of a new spectrometer (PHAROS) for these studies. Because the longitudinal velocity of sound is about 4300 m s^{-1}, a high incident neutron energy (0.187 eV) was required. Data have been obtained down to $Q \simeq 8$ nm^{-1} and $\hbar\omega = 25$ meV well inside the first pseudo-Brillouin zone of the glass. Evidence for two predominantly longitudinal excitations in the $Mg_{70}Zn_{30}$ glass is presented. Their positions agree approximately with theoretical predictions.

1. Introduction

By analogy with the Brillouin scattering of light, neutron Brillouin scattering (NBS) describes neutron inelastic scattering measurements made at momentum transfers $\hbar Q$ within the first Brillouin zone. Whereas conventional inelastic scattering experiments on crystals are generally performed in higher-order Brillouin zones to gain intensity and the results are presented after reduction to the first zone, the investigation of collective excitations (such as vibrations or magnetic excitations for example) in disordered matter is considerably more difficult, as no reciprocal lattice exists. However, provided these systems have short- and/or medium-range order, low-order pseudo-Brillouin zones can be defined close to the origin of reciprocal space. Here, the first maximum Q_p in the static structure factor $S(Q)$ can be regarded as the first, broadened reciprocal lattice point, such that the first pseudo-Brillouin zone extends up to $Q_p/2$ in reciprocal space [1].

An important role of NBS experiments is the investigation of the collective dynamics, by determining the dynamic structure factor $S(Q, \omega)$, for liquids and amorphous materials and the extraction of the single-excitation part $S_1(Q, \omega)$ of $S(Q, \omega)$, where $\hbar\omega$ is the experimentally observed energy transfer. This procedure is useful because the peaks in $S_1(Q, \omega)$, which contain information on the collective dynamical modes of the system, are more easily accessible to theory and more reliably interpreted. As Q increases these peaks become less pronounced, and at $Q > 2Q_p$ the structure of $S(Q, \omega)$ is dominated by the vibrational density of states, describing single-particle motion [1, 2]. A unique advantage of NBS experiments is their ability to distinguish between longitudinal and transverse excitations, as whilst neutrons couple directly to longitudinal vibrations they only couple to transverse vibrations via Umklapp-type processes outside the first Brillouin zone.

¶ Present address: Department of Physics, Oklahoma State University, Stillwater, OK 74078, USA.

0953-8984/95/254775+11$19.50

Such experiments place stringent kinematic constraints on the spectrometer, since they require a large ω range at the smallest Q values. A full picture of the dispersion curve necessitates the use of high neutron energies at scattering angles close to the straight-through beam, and there is a large amount of associated background and multiple scattering with few single scattering events [3].

The metallic glass $Mg_{70}Zn_{30}$ can be melt-spun in continuous ribbons, from which a suitable neutron scattering specimen may be made. Since the scattering amplitudes for Mg and Zn are similar (5.38 and 5.69 fm respectively) and the coherent scattering is about 98% of the total, it is a suitable sample for the investigation of collective excitations. We may represent, therefore, the scattering cross-section by an approximate formula

$$\frac{d^2\sigma}{d\Omega d\omega} = \bar{b}^2 \frac{k}{k_0} S(Q, \omega) \tag{1}$$

where $\bar{b}$ is the average scattering amplitude for Mg and Zn. Moreover, this glass has been the subject of investigation in previous experimental studies down to momentum transfers of 12 nm^{-1} at energy transfers of 28 meV, just inside the boundary of the first pseudo-Brillouin zone ($Q_p/2 = 13$ nm^{-1}) [4, 5]. In addition, there are extensive computer simulations using *a priori* pair potentials and other theoretical work [6].

Our previous experimental study of $Mg_{70}Zn_{30}$ on the HET spectrometer at the Rutherford Appleton Laboratory [4, 5] used 0.18 eV neutrons, and an angular range of 3.3° to 7°. The sample was enclosed in a multicellular cadmium grid, in which each cell was 6 mm square and 2 cm deep. This arrangement enhances the first scattering compared with multiple scattering processes. Data were taken near the boundary of the first pseudo-Brillouin zone. In order to extend the data further into this zone it is necessary to use an instrument that offers significantly lower scattering angles, and also to make an improved sample geometry. These were the technical objectives of the new experiment described here: in addition, we have begun a study of the temperature variations.

The intention of this paper is to present out NBS results on glassy $Mg_{70}Zn_{30}$ in which the accessible Q-range has been extended down to momentum transfers of 8.0 nm^{-1}. The new experimental conditions could be met by the new instrument [7], PHAROS, at the Los Alamos pulsed, spallation source facility (LANSCE). We employed a relatively high incident energy (0.187 eV or a neutron velocity of 6000 m s^{-1} compared with the velocity of longitudinal sound in the sample of 4300 m s^{-1}), and scattered angles down to 1°. (However, due to the low counting rates, we averaged several detectors giving a practical minimum of 2.87°.) Moreover, we have used a more sophisticated analysis of the data than was possible in the earlier experiments, since the majority of measurements were taken well inside the first Brillouin zone. These new data are compared to existing theoretical predictions [6]. A further goal of this experiment is to examine the variation of the spectral shape with temperature: for example, at room temperature the neutron scattering cross-section is higher than at low temperature (e.g. 100 K) where the excitation peaks may become sharper and better defined.

In section 2, the theoretical background will be presented briefly, and in section 3, the experimental samples and procedures will be described. This will be followed by sections on the data analysis and interpretation, and their comparison with published theoretical predictions.

2. Theoretical remarks

The structure (peaks and shoulders) of the single excitation part $S_1(Q, \omega)$ of the dynamic structure factor $S(Q, \omega)$ contains the information about the collective dynamics of the

atoms. Thus we separate this latter function into three parts as:

$$S(Q, \omega) = S_0(Q, \omega) + S_1(Q, \omega) + S_m(Q, \omega) \tag{2}$$

where S_0 represents elastic scattering and S_m represents the multi-excitation component. The (smallest) Q values which can be reached in an NBS experiment at a given ω depend on the scattering angle Θ and the incident energy E_0 or incident (k_0) and scattered (k) wavevectors necessary for the excitation of the modes. These quantities are related by the conditions for conservation of momentum and energy, namely,

$$Q^2 = k_0^2 + k^2 - 2kk_0\cos\theta \qquad \omega = \frac{\hbar}{2m}\left(k_0^2 - k^2\right) \tag{3}$$

where m is the neutron mass. They may be combined into the equation:

$$\hbar Q = \left[2m\left(E_0 - \hbar\omega\right) - 2\sqrt{E_0(E_0 - \hbar\omega)}\cos\Theta\right]^{1/2}. \tag{4}$$

In this section we assume that these equations yield values in the first pseudo-Brillouin zone of the $Mg_{70}Zn_{30}$ glass.

We start from $S_1(Q, \omega)$ for an elementary polycrystal with isotropic force constants and an atomic mass M, and scattering in the first Brillouin zone [8] i.e.

$$S_1(Q, \omega) = e^{2W}e^{\hbar\omega/2k_BT}\left[A\delta(Q - q)\delta\left(\omega - \omega_q\right)\rho\left(\omega_q\right)\right] \tag{5}$$

where

$$A = \frac{B\hbar Q^2}{4M\omega\sin h\left(\hbar\omega/2k_BT\right)}$$

and e^{-2W} is the Debye–Waller factor, (q, ω_q) are the wavenumber and frequency of a phonon in the first Brillouin zone, $\rho(\omega_q)$ is the density of states normalized to unit area and B is a dimensional factor. For a linear branch, with a sound velocity c, we would have $\omega_q = cq$. It is clear that for low values of Q the amplitude factor A is small and the density of states (which varies initially as ω_q^2) is also small. However, in this limit the product $A\rho(\omega)$ is independent of ω. Because these modes in a crystal are expected to be long-lived, they are represented as δ functions. For damped modes in an amorphous material, they might be represented as Lorentzian functions, with a peak width Γ proportional to Q^2 in the (small-Q) hydrodynamic limit. Provided that they have sufficient intensity, these peaks are therefore easiest to detect, and their width Γ is most reliably measured at the smallest momentum transfers. But in practice, the present experimental limitations have restricted our work to the peak positions only. To do this we need to subtract the multiphonon and multiple scattering intensities, by methods we shall describe in section 4.

3. Experimental details

The magnesium/zinc samples were fabricated from high-purity elements by melt-spinning. The sample container comprised a flat aluminium alloy frame container of volume 8.0 (height) × 5.5 (width) × 2.0 (depth) cm^3 intersected by a 6 mm × 6 mm square grid of 0.5 mm thick cadmium blades. Strips of the $Mg_{70}Zn_{30}$ melt-spun glass (of mass = 55.4 g

and mean density = 1.72 g cm^{-3}) were pressed into each of the 96 cells in the grid. Once loaded, the sample container was flushed for 30 minutes with helium gas before sealing, to avoid any additional background scattering from air left in the container.

Two experiments were performed on the $Mg_{70}Zn_{30}$ glass, at temperatures of 100 K and 297 K, using epithermal neutrons. An incident beam energy of 0.187 eV (close to the absorption maximum for neutrons in Cd) was chosen to provide a neutron velocity greater than the velocity of longitudinal sound, and to maximize the absorption of the grid and thereby reduce the large background of multiply-scattered neutrons. An identical grid was also used for the empty sample container run, and two halves of the same grid construction were placed either side of a 3 mm vanadium plate at room temperature for the calibration run. All sets of measurements were carried out under identical experimental conditions and temperature fluctuations were kept to within 0.5° between runs. The fast Fermi chopper (see [7]) for its characteristics) was run at 240 Hz for these experiments, giving a measured resolution of 10.5 meV FWHM at the elastic line, which was constant over the entire angular range. This frequency is slower than the optimum, giving broader than optimum resolution, a choice that was made to increase the observed intensity. We note that 5 meV corresponds to a timescale, given by $2\pi/\omega$, of 0.1 ps.

PHAROS [7] is a direct-geometry inelastic chopper spectrometer, purpose-built for NBS experiments requiring high-ω-resolution, low-angle work (in another mode it can also be used for high-angle, high-resolution work). It has a water moderator poisoned with gadolinium places near the spallation target, and a 20 m incident flight path (see figure 1). Two mechanical choppers are installed in the incident beam. At 14 m from the moderator, a double-bladed chopper, rotating at 120 Hz (the fundamental frequency of the linear accelerator) is employed to suppress the high-energy neutron background. Downstream (at 18 m) the high-speed Fermi chopper (referred to above) is phased with the accelerator pulse to select the required incident neutron energy.

A boron carbide mask defined the incident beam of 7.5 cm × 5.0 cm at the sample position, and the scattered neutrons travelled a further distance of 5.75 m along the secondary path before reaching the detector plane. The detector grid comprised five banks of linear position-sensitive ^{3}He detectors, each consisting of eight, one inch diameter and 36 inch long detectors mounted vertically. For convenience, this arrangement was asymmetric in the horizontal plane with two banks located on each side of the incident beam (covering angles from 1.3° to 5.4° and 3.5° to 6.9°, separately), with an additional single bank covering the angles between 5.8° to 8.8° on one side. In total, this gave an angular range of 1.3° to 8.8° in the forward scattering direction and with the vertical position sensitivity gave an x–y distribution of data points. The detector distribution for the experiment is illustrated in figure 2. Detector calibration measurements performed before and after the experiment showed a high degree of detector stability throughout the experiment. Due to the relatively low flux at high incident energies, low scattering angles and attenuation of the scattered beam by the cadmium grid, sample run times of 9 days at 100 K and 4.5 days at 297 K were required to obtain useful statistics on the summed data. (A longer run at 297 K would have been desirable but was not possible.)

The pixels of the x–y detector were grouped into four rings centred at zero degrees. The (ω–Q) profiles for these constant-Θ rings are shown in figure 3, together with theoretical curves for the two longitudinal modes in $Mg_{70}Zn_{30}$ glass (see Hafner [6], figure 6). From an experimental viewpoint the situation is very favourable as the ω–Q rings intersect with the theoretical dispersion curves at an angle close to 90°. In addition, the width of each ring is only spread over a <2 meV range when intersecting either of the two dispersion

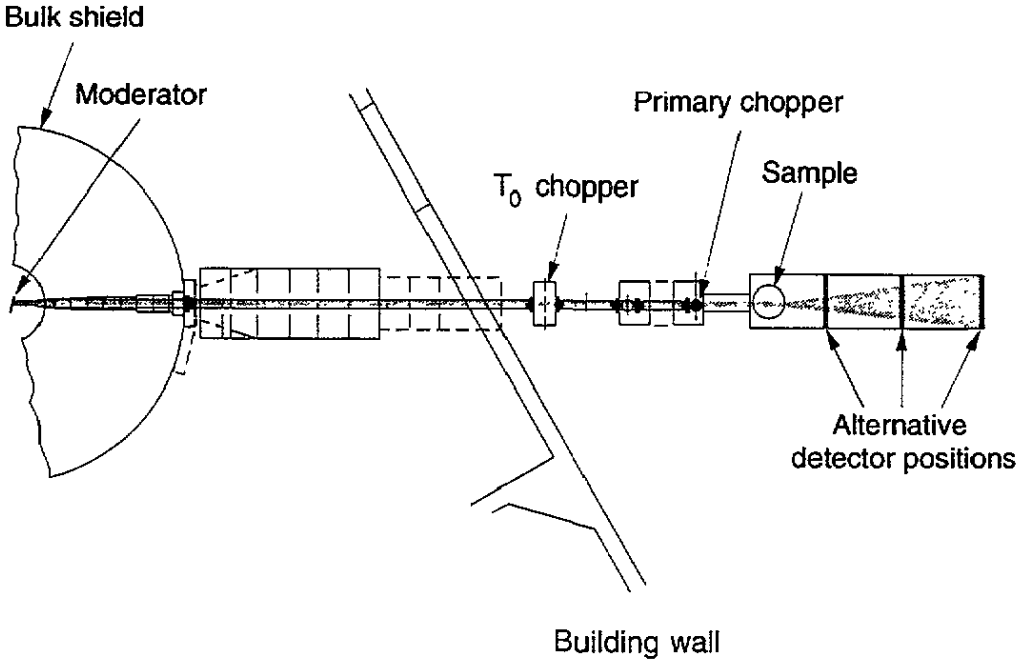

Figure 1. A schematic diagram of the initial set-up for the PHAROS spectrometer at Los Alamos. Full details can be found in [7].

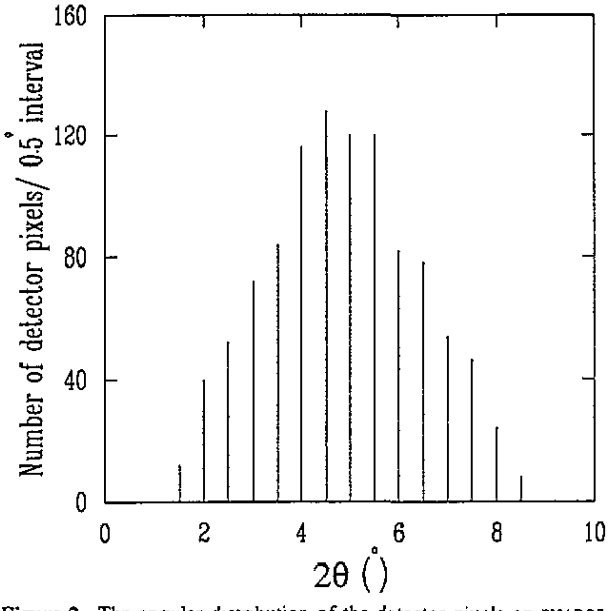

Figure 2. The angular distribution of the detector pixels on PHAROS for this experiment. The decrease beyond 5° is due to the limited size of the rectangular detector array.

curves shown in figure 3. The ringed data sets were converted from time-of-flight onto an

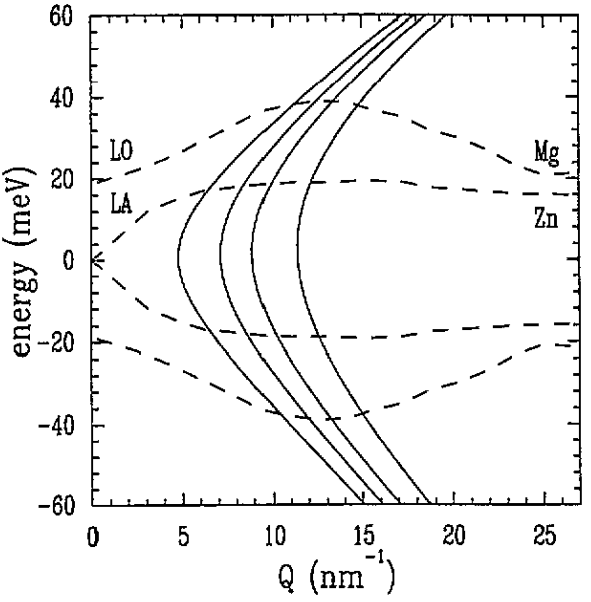

Figure 3. The four cuts in ω–Q space along which x–y data were collected into constant-angle data (solid lines). The dashed lines correspond to the theoretical curves for the two longitudinal modes (see text) calculated by Hafner ([6] figure 6) for the metallic glass $Mg_{70}Zn_{30}$. (LA=longitudinal acoustic; LO=longitudinal optic).

energy scale, the backgrounds subtracted and analysed using a two-stage process.

4. Analysis of data

In the first stage of the analysis, the ringed data were rebinned in energy onto a linear scale using 2.0 meV bins. A correction for neutron capture efficiency in cylindrical detectors was made [9], and the data sets normalized to the ringed vanadium spectra using the number of counts under the vanadium elastic peak. An energy-independent correction of the type described in [10] was applied to the data and empty container scattering using the equation

$$I_{\mathrm{corr}} = \frac{I_{\mathrm{S+C}}}{A_{\mathrm{S,SC}}} - M\frac{A_{\mathrm{C,SC}}}{A_{\mathrm{C,C}}A_{\mathrm{S,SC}}}I_{\mathrm{C}} \tag{6}$$

where I_{corr} is the corrected intensity. $I_{\mathrm{S+C}}$ and I_{C} denote the measured intensities of the sample plus container and smoothed empty container runs respectively. $A_{\mathrm{S,SC}}$, $A_{\mathrm{C,SC}}$ and $A_{\mathrm{C,C}}$ are the corresponding absorption correction factors calculated for flat-plate geometry, and M is the monitor count ratio of the two runs.

For the second stage, a two-channel maximum entropy method [11] was used to separate out the relatively sharp, single-excitation scattering events from the large multiply-scattered and multi-excitation background. The maximum entropy algorithm creates two channels; one is designed to accept only sharp features i.e. the peaks (see equation 2) corresponding to the required $S_0(\Theta, \omega) + S_1(\Theta, \omega)$, whilst the other accepts only broad structure i.e. $S_m(\Theta, \omega)$. Our experimental data will be presented as constant θ results, and the relationship

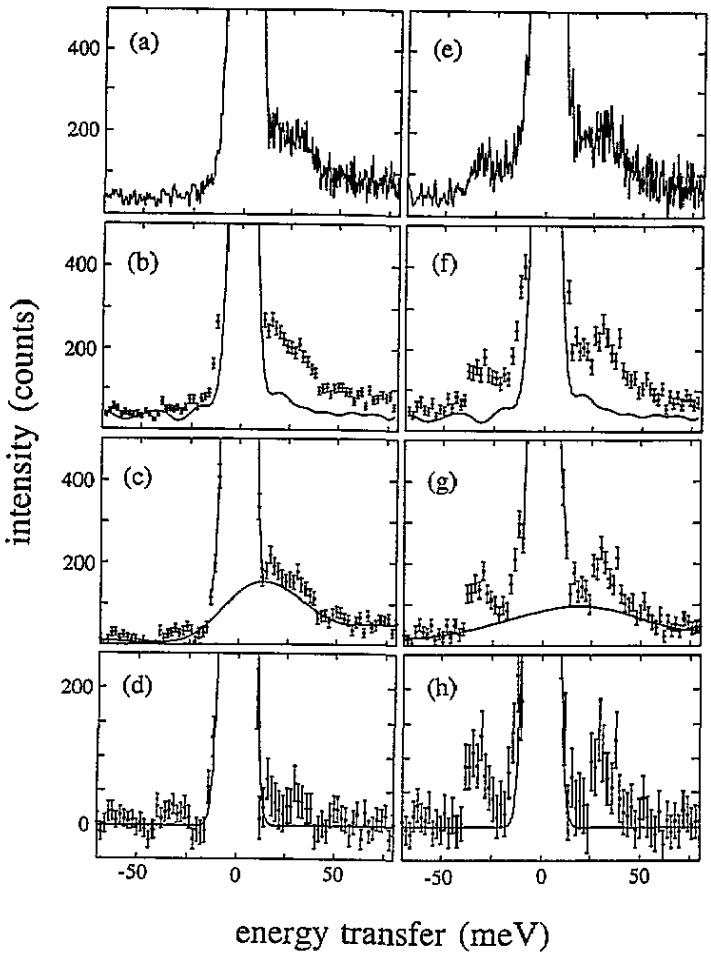

Figure 4. Step in data handling for $\Theta = 5.35°$ at temperatures of 100 K ((*a*) to (*d*)) and 297 K ((*e*) to (*h*)), respectively. (*a*) and (*e*): initial spectra corrected for detector efficiency and normalized to vanadium. (*b*) and (*f*): rebinned energy spectra for sample plus can and smoothed empty can runs. (*c*) and (*g*): sample-only spectra and broad maximum entropy component. (*d*) and (*h*): $S_1(\Theta, \omega) + S_1(\Theta, \omega)$ for the $Mg_{70}Zn_{30}$ glass (error bars) and $S_0(\Theta, \omega)$ (line) obtained from the vanadium spectra.

between $S_1(\Theta, \omega)$ and $S_1(Q, \omega)$ for example, may be obtained readily from equations such as (4) and (5). It was expected that the multiple-scattering and multi-excitation contributions (which include both multiple and single scattered multiphonon terms) would dominate the broad part of the spectra. To aid in the analysis, the following constraints were imposed on the two channels: the broad component should be smoothly varying with the ends of the spectra decreasing to a constant value, and the excitation peak area in the sharp spectra should increase as Q^2 (see section 2). Thus the lowest angular spectra taken at an average angle of $\Theta = 2.87°$ were fitted assuming virtually all the inelastic scattering was due to multiple scattering. The width of the angular rings ranged from $\Delta Q = 1.5$ nm^{-1} for the middle two angular rings to about 3.9 nm^{-1} for the highest angular ring. At each angle, a comparison of the broad components at both temperatures showed them to be similar in shape, although the $T = 297$ K data are greater in intensity on the neutron energy gain side

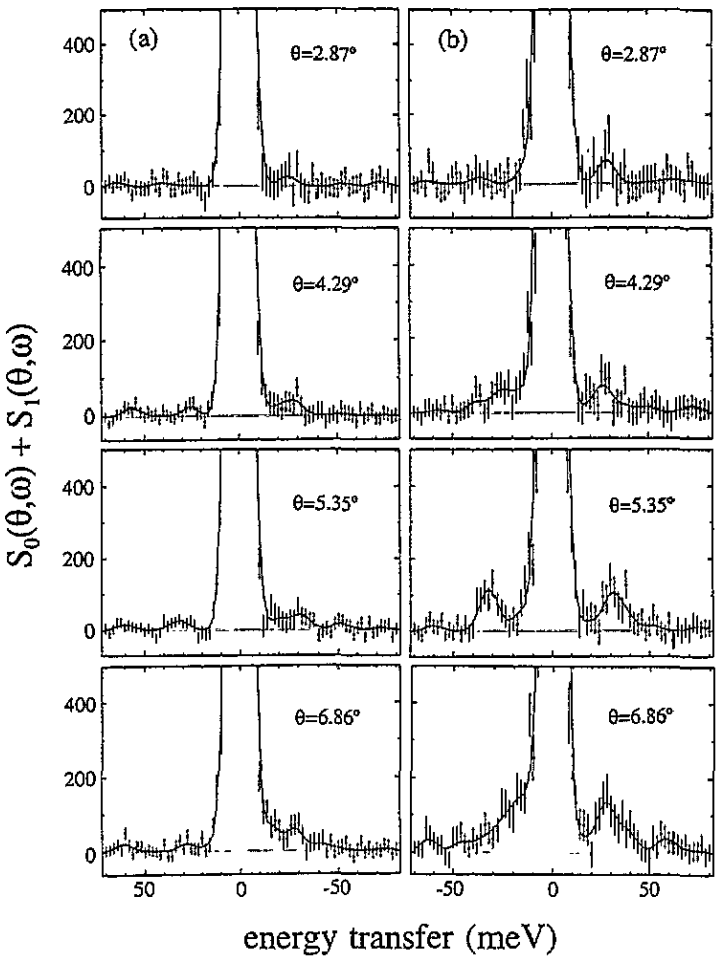

Figure 5. $S_0(\Theta, \omega) + S_1(\Theta, \omega)$ (see equation 2) spectra for $Mg_{70}Zn_{30}$ at (*a*) 100 K and (*b*) 297 K derived by collecting x–y data into angular groups and interpreting by the maximum entropy method. The points (with error bars) represents the experimental data while the solid line represents the maximum entropy fit to the data (see [10]).

as expected. Moreover, both temperature runs showed a strong angular dependence of the broad component, a possible effect of the cadmium grid in reducing the multiple scattering below the level of the multi-excitation processes. These broad spectra were subtracted from the original four data sets to give the function $S_0(\Theta, \omega) + S_1(\Theta, \omega)$ (measured at fixed scattering angle Θ).

Figure 4 shows this process at both temperatures; the original data, the rebinned data and the separation into broad and structured components are illustrated. Figure 5 shows the $S_0(\Theta, \omega) + S_1(\Theta, \omega)$ data points with the most likely smooth line through the data. Differences taken between detector rings (at the same and different temperatures) showed little structure above the statistical noise, which suggested the presence of a plateau in the dispersion curve which is evident when the (ω, Q) relationship for the observed peak positions is plotted in figure 6.

An alternative interpretation may be made by calculating the density of states function

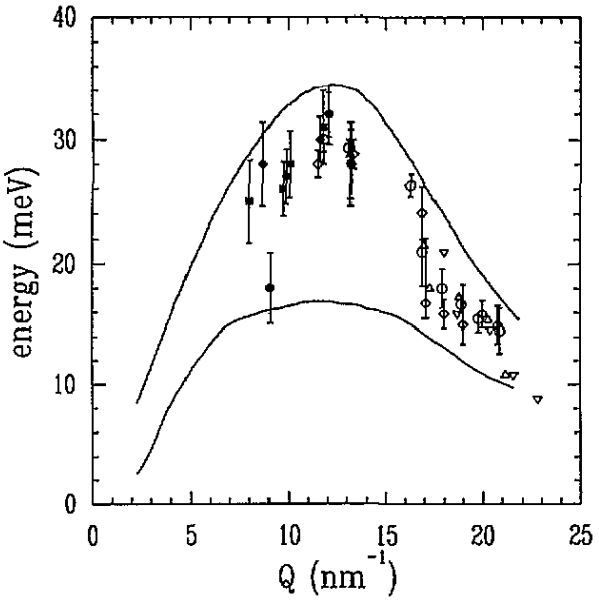

Figure 6. An ω–Q plot for the peaks in $S_1(\Theta, \omega)$ for the metallic glass $Mg_{70}Zn_{30}$. The results of the present investigation are shown as solid diamonds and squares for the 297 K run and 100 K run, respectively. The solid circle denotes the lower beak position obtained from the $f_1(\Theta, \omega)$ function shown in figure 7. The open symbols correspond to the previous results on the same metallic glass made on the IN4, IN6 and HET spectrometers [4, 5]. The top line corresponds to the theoretical peak positions in $S_1(\Theta, \omega)$, calculated by J-B Suck (see Egelstaff [12] figure 3). The bottom line corresponds to the dispersion relation for the 'longitudinal acoustic' mode calculated Q by Hafner (see [6] figure 6). The error bars shown on our data are a combination of the variation in Q arising from the finite width of the angular ring and the shape of the resolved peak in $S_1(\Theta, \omega)$.

$f'(Q, \omega)$ as in [6]. If we assume there is no incoherent contribution, then by using equation (3) of [4], this quantity may be written, where c_i and M_i are the concentration and mass of component i, as:

$$f'(Q, \omega) = \sum e^{-2W} \frac{f_{\alpha\beta}(Q, \omega) c_\alpha c_\beta}{\sqrt{M_\alpha M_\beta}} \tag{7a}$$

where

$$f_{\alpha\beta}(Q, \omega) = \frac{\omega(1 - e^{-\hbar\omega/k_B T})}{\hbar Q^2} S^1_{\alpha\beta}(Q, \omega) \ldots \tag{7b}$$

and $S^1_{\alpha\beta}$ is the single-excitation partial dynamic structure factor $f'(Q, \omega)$ will denote a weighted sum of $f_{\alpha\beta}(Q, \omega)$ partials, and $f_1(Q, \omega)$ will denote the similar weighted sum using constant angle data in place of constant Q data. These functions are shown in figure 7. For our case, the Debye–Waller factor was calculated to be very close to unity (using equation (3.63) in [8]). The advantages of this presentation are that it emphasizes the energy transfer intensity distribution, and that a theoretical predication is available in [6] (figure 4 of [6]). In order to separate $f_1(\theta, \omega)$, the elastic peak contribution to the spectra, $S_0(\theta, \omega)$ needed to be subtracted from the spectra shown in figure 5. $S_0(\theta, \omega)$ was

obtained by fitting the elastic peak of the vanadium spectra with a Gaussian distribution (see figures 4(*d*) and 4(*h*)). To improve our statistics, we have added together the $f_1(\theta, \omega)$ spectra for both the 4.29° and 5.35° rings (these angles were chosen as they have the best θ resolutions) and both temperatures. Finally, the comparison of the experimental and theoretical functions is shown at figure 7.

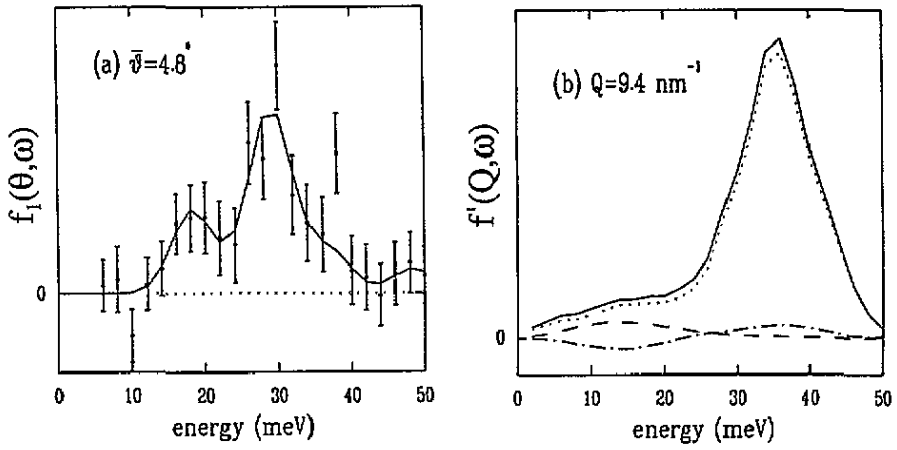

Figure 7. A comparison of the $f'(Q, \omega)$ function calculated from the sum of individual $f_{\alpha\beta}(\theta, \omega)$ functions taken from [6] and shown in 7(*b*), and the function $f_1(\theta, \omega)$ (full line in 7(*a*)) derived from our data at angles of 4.29°, 5.35° and both temperatures combined. The individual partial dynamic structure factors are represented by $f_{MgMg}(Q, \omega)$ (dotted line), $f_{ZnZn}(Q, \omega)$ (dashed line), $f_{MgZn}(Q, \omega)$ (chain line) shown in (*b*) and the solid line in (*a*) is a fit to the experimental data. The two curves in 7(*a*) (from experiment) and (*b*) (from theory) have not been drawn to the same scale.

5. Discussion and conclusions

It can be seen in figures 5(*a*) and (*b*) that $S_1(\theta, \omega)$ exhibits a single-excitation peak even at the lowest angle in both the 100 K and 297 K data sets. Furthermore, despite the shorter run time, the greater count rate associated with the single-excitation peaks in the room temperature experiment is clearly illustrated, especially at the largest angles. The ratio of the areas of the measured single-excitation peak at the two temperatures is also in reasonable agreement with those values calculated from an isotropic Einstein model of the glass given by equation (5). The high signal/background ratio obtained on PHAROS and an improved data treatment process have yielded overall better data compared with our previous experiments [4, 5], although the energy resolution is worse.

From the data in figure 5, the peak positions (in ω and Q) have been extracted and are plotted in figure 6. Also shown in this figure are our earlier data identified as a longitudinal mode in the $Mg_{70}Zn_{30}$ glass [4, 5], and it can be seen that the new and old data are in good agreement. The new data also extend significantly further into the first zone. The solid lines in this figure are based on the calculation by Hafner [6] of the two longitudinal modes: as in our earlier work, we estimated the theoretical peak positions in $S_1(\theta, \omega)$ from Hafner's results. Only at the lowest momentum transfers (calculated to be $Q \leqslant 3.1$ nm^{-1} in [6])

can the acoustic and optic modes (as defined by Hafner) be clearly identified. For larger Q values, towards the zone boundary ($Q \geqslant 6.2$ nm^{-1} in [6]) it has been predicted that the acoustic optic modes will tend to be dominated by the vibrations of the Zn and Mg atoms, respectively.

The main phonon intensity measured in this study is therefore expected to be due to the longitudinal 'optic' mode which mainly corresponds to the vibrations of the lighter Mg atoms. There will also be a less intense phonon peak at lower energy transfers, close to the elastic peak, primarily due to the Zn atomic vibrations (i.e. the longitudinal 'acoustic' mode) e.g. see figure 7(a). This explanation is the simplest interpretation of the present results i.e. that two peaks are found in the spectra at around 18 meV and 30 meV. Due to the experimental set-up, there is a finite band of Q values over which the phonon peak energies were averaged: however, this phenomenon does not alter the overall results of this experiment. The broader peaks observed at higher energy transfers in figure 5 ($E \geqslant 40$ meV) are probably due to residual multiphonon effects; a full calculation of the expected $S(Q, \omega)$ intensity is required for a detailed description of this ω region.

The comparison shown in figures 7(a) and (b) suggests that a larger contribution from the Zn–Zn correlations is seen experimentally than is predicted by theory. In addition, the peak positions are not in full agreement, which suggests that the small discrepancy between theory and experiment in figure 6 may be real.

It is concluded that a modern NBS instrument can extend the data on high velocity of sound materials (e.g. $Mg_{70}Zn_{30}$) into the first Brillouin zone. In this way, the nature of the modes can be identified positively and excellent comparisons with theoretical predictions (based on fundamental information) may be attempted.

Acknowledgments

We would like to acknowledge the assistance of P S Lysaght, E Larson and J P Sandoval during the course of our experiments, and the advice of Dr D S Sivia during the maximum entropy processing. We are also grateful to the NATO Collaborative Research Grants Program for a travel grant and to the NSERC of Canada for their financial support of the Canadian participants. This work was funded in part by the division of Basic Energy Sciences of the US Department of Energy.

References

[1] Suck J-B, Rudin H, Güntherodt H-J and Beck H 1983 *Phys. Rev. Lett.* **50** 49
[2] Suck J-B, Rudin H, Güntherodt H-J and Beck H 1980 *J. Phys. C: Solid State Phys.* **13** L1045, 1981 **14** 2305
[3] Robinson R A 1989 *Advanced Neutron Sources 1988 (IOP Conf. Ser. Topics in Applied Physics)* p 311
[4] Suck J-B, Egelstaff P A, Robinson R A, Sivia D S and Taylor A D 1992 *Europhys. Lett.* **19** 207
[5] Suck J-B, Egelstaff P A, Robinson R A, Sivia D S and Taylor A D 1992 *J. Non-Cryst. Solids* **150** 245
[6] Hafner J 1983 *J. Phys. C: Solid State Phys.* **16** 5773
[7] Robinson R A, Nutter M, Ricketts R L, Larson E, Sandoval J P, Lysaght P S and Olivier B J 1993 *Proc. ICANS-XII, Rutherford Appleton Laboratory Report RAL 94-025* vol I, p 44
[8] Squires G L 1978 *Introduction to the Theory of Thermal Neutron Scattering* (Cambridge University Press)
[9] Windsor C G 1981 *Pulsed Neutron Scattering* (London: Taylor Francis)
[10] Soper A K and Egelstaff P A 1980 *Nucl. Instrum. Methods* **178** 415
[11] Sivia D S 1990 *Maximum Entropy and Bayesian Methods* ed P Fougere (Netherlands: Kluwer) p 195
[12] Egelstaff P A 1992 *J. Phys. C: Solid State Phys.* **156–158** 1–8